Correction of Periodic Motion Artifacts Along the Slice Selection Axis in MRI

T. MITSA, K. J. PARKER, SENIOR MEMBER, IEEE, W. E. SMITH, A. M. TEKALP, MEMBER, IEEE, AND J. SZUMOWSKI

***Abstract*—In magnetic resonance imaging (MRI), periodic motion such as normal breathing, causes artifacts that are primarily manifested as "ghost" images in the phase encoding direction of the image. In this paper, we model the effect of periodic motion of a single slice in the direction of the slice selection axis as amplitude modulation of the raw data with a motion kernel along the phase encoding direction in the Fourier domain. We show that this motion can be detected in 1-D projections of the raw data along the frequency encoding direction, which in combination with appropriate filtering leads to the recovery of the motion kernel. Finally, we demonstrate, by means of simulation examples, that significant reduction in the amplitude of the ghost artifacts is obtained, when we filter the image by the inverse of the motion kernel. Some issues to be investigated before the technique can be used in a clinical environment are mentioned.**

I. Introduction

In MRI, single plane and multiple plane data acquisition can last several minutes, which makes the technique sensitive to tissue motion and blood flow. Periodic motion such as breathing produces undesirable blurring and "ghost" images or periodic replications of moving anatomic structures. The ghost images can overlap with other structures, obscure abnormalities, and generally degrade the diagnostic content of the images. A theoretical model for periodic motion artifacts was first developed by M. L. Wood [1]. He demonstrated that motion in any of the three axes (x, y, z) creates ghost artifacts along the phase encoding direction in two-dimensional (2-D) Fourier transform imaging.

The artifact suppression methods that have been reported in the literature so far are instrumental techniques related to novel data acquisition schemes such as ordered phase encoding and gradient waveform modification [2], [3]. A review of some artifact suppression techniques is given in [4]. An algorithmic approach which requires the use of specially encoded "navigator" echoes has been reported recently [5]. The method proposed in this paper is novel in that it is an algorithmic post-processing technique for periodic motion artifact suppression, and does not require monitoring of the motion.

In this paper, we examine periodic motion along the z (slice selection) axis and model its effects as amplitude modulation of the raw data by a motion kernel along the phase encoding direction. The model assumes slow periodic movement of a single slice in the z-direction. This is a simplification of the actual phenomenon in that our model ignores the effect of the structures above and below this slice. A study to include these effects into the model is being conducted. We review the principles of 2-D Fourier transform (spin-warp) MRI in Section II.A. In Section II.B, we develop a new model for the effect of periodic motion in the slice selection direction on MRI. Based on this model, we propose a new algorithm for the detection of the motion parameters and the correction of the corresponding motion artifacts in Section II.C. We demonstrate the feasibility of the proposed algorithm with simulation examples in Section III.

II. Theory

A. Principles of 2-D Fourier Imaging

A very common MRI data acquisition technique and also the one used in this paper is 2-D Fourier imaging [6], [7]. In this method, it is the Fourier transform of the final image which is actually measured during the acquisition. The pulse sequence commences with the simultaneous application of a 90 degree RF pulse and a z gradient G_z, which results in the selection of a slice (Fig. 1).

After the slice has been selected, the signal must be spatially encoded in the x and y directions within the slice. A second gradient (G_x) applied along the x direction permits positions along this direction to be frequency encoded. A third gradient (G_y) applied along the y direction, permits positions along this direction to be phase encoded, i.e., it assigns specific phase to the precessing nuclei as a function of y-direction.

A spin echo is recorded following the reverse G_x pulse as shown in Fig. 1. The process is repeated with a different G_y every T_R seconds until sufficient phase encoding steps are recorded.

Assume that a stationary point source exists at (x_0, y_0, z_0) and it has intrinsic strength m_0. The actual strength of the point source is $m_0 \bar{m}(z_0)$ where $\bar{m}(z_0)$ is the excitation cross section of the slice. The excitation cross section of

Manuscript received January 12, 1990; revised January 27, 1990. This work was supported in part by the University of Rochester, Departments of Electrical Engineering, Radiology, and Institute of Optics, and by the Joint Services Optics Program.

T. Mitsa and A. M. Tekalp are with the Department of Electrical Engineering, University of Rochester, Rochester, NY 14627.

K. J. Parker is with the Departments of Electrical Engineering and Radiology, University of Rochester, Rochester, NY 14627.

J. Szumowski is with the Department of Radiology, Oregon Health Sciences University, Portland, OR 97201

W. E. Smith is with the Institute of Optics, University of Rochester, Rochester, NY 14627.

IEEE Log Number 9035089.

0278-0062/90/0900-0310$01.00 © 1990 IEEE

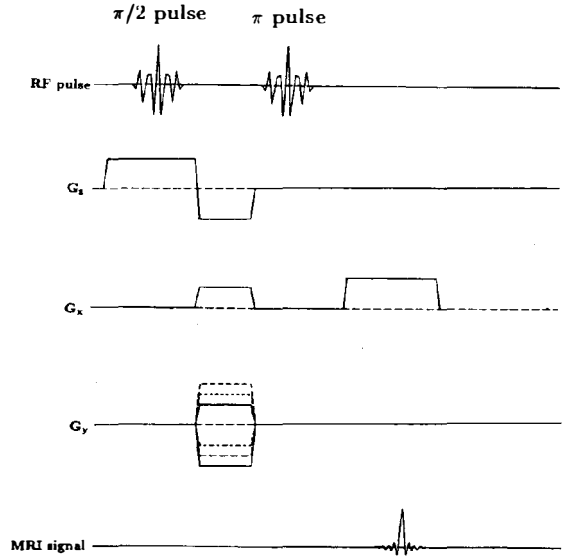

Fig. 1 Pulse sequence.

the slice depends upon the shape of the gradient of the magnetic field and upon the spectrum of the RF excitation pulse.

Defining as N_y the number of phase encoding steps, N_x the number of frequency encoding steps, and γ the gyromagnetic ratio, the acquired MRI signal can be written as following [1]:

$$S(t, G_y, z_0) = m_0 \tilde{m}(z_0)\, E_x(t)\, E_y(G_y) \cdot \exp\left\{\left(-2\pi i\left[\left(-\frac{\gamma}{2\pi} G_x x_0\right)t + \left(\frac{\gamma}{2\pi} t_y y_0\right) G_y\right]\right)\right\} \times \operatorname{comb}\left(\frac{t}{\Delta t}, \frac{G_y}{\Delta G}\right) \operatorname{rect}\left(\frac{t}{N_x \Delta t}, \frac{G_y}{N_y \Delta G}\right) * \operatorname{comb}\left(\frac{t}{N_x \Delta t}, \frac{G_y}{N_y \Delta G}\right) \quad (1)$$

where $E_x(t)$ and $E_y(t)$ are apodization functions and $*$ denotes convolution. For the sake of convenience we will ignore in the following the apodization, rect, and comb terms because we assume that the relaxation and sampling effects do not contribute to the analysis. Thus $S(t, G_y, z_0)$ can be written as:

$$S(t, G_y, z_0) = m_0 \tilde{m}(z_0) \exp\left\{\left(-2\pi i\left[\left(-\frac{\gamma}{2\pi} G_x x_0\right)t + \left(\frac{\gamma}{2\pi} t_y y_0\right) G_y\right]\right)\right\}. \quad (2)$$

Defining as $K_x = -(\gamma/2\pi) G_x t$ and $K_y = (\gamma/2\pi) t_y G_y$ the axes in the raw data domain, (2) can also be written as follows:

$$S(K_x, K_y, z_0) = m_0 \tilde{m}(z_0) e^{(-iK_x x_0)} e^{(-iK_y y_0)}. \quad (3)$$

B. Model for Periodic Motion Along the Slice Selection Axis

Now we assume that the point source is moving periodically in the z direction and represent its motion by the function $z(T)$ where T is the motion time variable. Expanding in a Fourier series:

$$z(T) = \sum_{n=-\infty}^{\infty} c_n e^{(2\pi i n f_0 T)} \quad (4)$$

where $f_0 = 1/\tau$ with τ the period of the motion. The complex coefficients c_n are given by

$$c_n = \int_t^{t+\tau} z(a) e^{(-2\pi i n f_0 a)}\, da. \quad (5)$$

Because z itself is a function of time T for our moving point source, we can write an expression for the magnetization of the source as a function of time:

$$m(T) = \tilde{m}(z(T)). \quad (6)$$

Because this new function is also periodic we can also write it as a Fourier series:

$$m(T) = \sum_{n=-\infty}^{\infty} d_n e^{(2\pi i n f_0 T)} \quad (7)$$

with an expression for the new coefficients d_n similar to that of equation (5) with the integral now over $m(a)$. Setting $d_0 = 1$, $d_n = (\Delta m_n/2m_0) e^{(i\phi_n)}$, $d_{-n} = (\Delta m_{-n}/2m_0) e^{(-i\phi_n)}$ equation (7) becomes:

$$m(T) = 1 + \sum_{n=1}^{\infty} \frac{\Delta m_n}{m_0} \cos(2\pi n f_0 T + \phi_n) \quad (8)$$

where Δm_n refers to change in mass due to the nth harmonic of the periodic motion. Substituting $m(T)$ in (3), the expression for the acquired MRI signal for a moving point source becomes:

$$S(K_x, K_y, T) = m_0 m(T) e^{(-iK_x x_0)} e^{(-iK_y y_0)} = (m_0 e^{(-iK_x x_0)} e^{(-iK_y y_0)}) \cdot \left[1 + \sum_{n=1}^{\infty} \frac{\Delta m_n}{m_0} \cos(2\pi n f_0 T + \phi_n)\right]. \quad (9)$$

We assume that $\Delta m_n/m_0$ is less than unity so $m(T)$ is always positive and ϕ_n is the phase of the breathing with respect to the start of data acquisition for the nth harmonic. In this paper, we will assume that the motion of the source is slow compared to data acquisition rates along the frequency x-gradient, but that the motion is not slow between y-axis phase encodings. The motion time T and

K_y (or G_y) are connected through the following equation [2]:

$$T = \frac{K_y}{\Delta K} T_R \tag{10}$$

where ΔK are the steps by which K_y is incremented and T_R is the time between phase encoding steps. This equation transforms the independent variable in (8) from T to K_y.

With this change of variables, we may write:

$$m(K_y) = 1 + \sum_{n=1}^{\infty} \frac{\Delta m_n}{m_0} \cos\left(\frac{2\pi n N_b K_y}{N_y \Delta K} + \phi_n\right) \tag{11}$$

where $N_b = f_0 N_y T_R$ is the number of breathing cycles per entire scan. After the change of variables, equation (9) becomes:

$$\begin{aligned} S(K_x, K_y) &= m_0 m(K_y) e^{(-iK_x x_0)} e^{(-iK_y y_0)} \\ &= (m_0 e^{(-iK_x x_0)} e^{(-iK_y y_0)}) \\ &\quad \cdot \left[1 + \sum_{n=1}^{\infty} \frac{\Delta m_n}{m_0} \cos\left(\frac{2\pi n N_b K_y}{N_y \Delta K} + \phi_n\right)\right]. \end{aligned} \tag{12}$$

The final image $I(x, y)$, is the inverse Fourier transform of the collected data:

$$I(x, y) = \int_{K_x} \int_{K_y} S(K_x, K_y)\, dK_x\, dK_y. \tag{13}$$

Replacing $S(K_x, K_y)$ from (12), (13) can be written as:

$$I(x, y) = \int_{K_x} \int_{K_y} m_0 m(K_y) e^{(iK_x(x - x_0))} e^{(iK_y(y - y_0))}\, dK_x\, dK_y. \tag{14}$$

Performing the integration over K_x in (14) we get

$$I(x, y) = \delta(x - x_0) \int_{K_y} (m_0 m(K_y) e^{(-iK_y y_0)}) e^{(iK_y y)}\, dK_y. \tag{15}$$

The above integral is actually the inverse Fourier transform of the product $m(K_y) e^{(-iK_y y_0)}$. According to the convolution and shift properties of Fourier transform pairs, the above equation can be written as

$$I(x, y) = \delta(x - x_0)\left(\left[\int_{K_y} m_0 m(K_y) e^{(iK_y y)}\, dK_y\right] * \delta(y - y_0)\right). \tag{16}$$

Replacing $m(K_y)$ from (11) $I(x, y)$ becomes

$$\begin{aligned} I(x, y) &= \int_{K_y} m_0 e^{(iK_y y)}\, dK_y + \sum_{n=1}^{\infty} \int_{K_y} \Delta m_n \\ &\quad \cdot \cos\left(\frac{2\pi n N_b K_y}{N_y \Delta K}\right) e^{(iK_y y)}\, dK_y \\ &= m_0 \delta(y) + \sum_{n=1}^{\infty} \frac{\Delta m_n}{2} e^{(i\phi_n)} \delta\left(y + \frac{n N_b}{N_y \Delta K}\right) \\ &\quad + \sum_{n=1}^{\infty} \frac{\Delta m_n}{2} e^{(-i\phi_n)} \delta\left(y - \frac{n N_b}{N_y \Delta K}\right). \end{aligned} \tag{17}$$

Therefore, $I(x, y)$ consists of an impulse at the origin plus smaller and phase shifted "ghost" impulses at a and $-a$ where $a = nN_b/N_y \Delta K$. Thus the ghosts will appear only along the phase encoding direction and their distance depends upon how many breathing cycles occur during the data acquisition.

We now replace the point source with a stationary infinitely thin object $m_b(x, y)$ within the field of view. If the entire object plane is moving periodically in the z direction, then from (12) by replacing x_0, y_0 with x, y and integrating over x, y space the acquired signal $S(K_x, K_y)$ will be:

$$\begin{aligned} S(K_x, K_y) &= \int_{-\infty}^{\infty} m_b(x, y) e^{-i(K_x x - K_y y)}\, dx\, dy \\ &\quad \times \left[1 + \sum_{n=-\infty}^{\infty} \frac{\Delta m_n}{m_0} \cdot \cos\left(\frac{2\pi n N_b K_y}{N_y \Delta K} + \phi_n\right)\right] \end{aligned} \tag{18}$$

$$\begin{aligned} S(K_x, K_y) &= M(K_x, K_y)\left[1 + \sum_{n=-\infty}^{\infty} \frac{\Delta m_n}{m_0} \cdot \cos\left(\frac{2\pi n N_b K_y}{N_y \Delta K} + \phi_n\right)\right] \end{aligned} \tag{19}$$

where by $M(K_x, K_y)$ we denote the Fourier transform of $m_b(x, y)$. Note that $m_b(x, y)$ denotes the artifact-free image. We can also write (19) as:

$$S(K_x, K_y) = M(K_x, K_y)\left[1 + \sum_{n=1}^{\infty} \frac{\Delta m_n}{m_0} \cdot \cos\left(\frac{n\omega_y K_y}{N_y} + \phi_n\right)\right] \tag{20}$$

where $\omega_y = 2\pi N_b/\Delta K$.

C. Estimation of the Motion Kernel and Correction of the Motion Artifact

Equation (20) indicates that the z-motion causes a modulation of the measured data in the K_y direction. We at-

tempt to correct for this modulation by essentially estimating specific frequencies along K_y at which excess power is located and then suppressing the power at such frequencies.

The detection and removal of the amplitude modulation (the term in brackets in equation (20)), is done in the following steps:

1) We project the magnitude of the raw data along the frequency encoding direction. Let P_M denote a projection of the magnitude of $M(K_x, K_y)$ as follows:

$$P_M(K_y) = \int_{-\infty}^{\infty} \left| M(K_x, K_y) \right| dK_x, \tag{21}$$

then the projection of the magnitude of the raw data can be expressed as:

$$\begin{aligned} P_S(K_y) &= \int_{-\infty}^{\infty} \left| S(K_x, K_y) \right| dK_x \\ &= P_M(K_y)\left[1 + \sum_{n=1}^{\infty} \frac{\Delta m_n}{m_0} \cos\left(\frac{n\omega_y K_y}{N_y} + \phi_n \right) \right] \end{aligned} \tag{22}$$

where the last line substitutes from (20) and (21).

2) We define the inverse Fourier transform of the projection $P_M(K_y)$ as:

$$p_M(y') = \int P_M(K_y) e^{iK_y y'} dK_y \tag{23}$$

then from (22) and (23) the inverse Fourier transform of the projection of the magnitude of the raw data is

$$\begin{aligned} p_S(y') &= \int P_S(K_y) e^{iK_y y'} dK_y \\ &= p_M(y') * \left[\delta(y') + \sum_{n=1}^{\infty} \frac{\Delta m_n}{2m_0} e^{i\phi_n} \delta(y' + nf_y) \right. \\ &\quad \left. + \sum_{n=1}^{\infty} \frac{\Delta m_n}{2m_0} e^{-i\phi_n} \delta(y' - nf_y) \right] \end{aligned} \tag{24}$$

where $f_y = \omega_y / 2\pi$ and the prime on y indicates that we have not returned to the original image space by virtue of the projection and magnitude operations.

Our ability to detect in projections the motion-kernel frequencies is based on the following assumptions:

(a) The effect of the motion in the raw data domain can be modeled reasonably well with finitely many terms in (8), (*b*) $p_M(y')$ is highly peaked around the DC term with other frequencies at least two orders of magnitude below, since $P_M(K_y)$ is a magnitude projection and a slowly varying function of K_y.

An example is shown in Figs. 2 and 3. As (24) shows, the effect of the motion in the inverse Fourier transform of the projection is additional impulses, where the magnitude and frequency provide information concerning the location and frequency of the breathing artifact. Based on the previous assumptions, in this paper we attribute to motion those peaks in the magnitude of $p_S(y')$, that are at least two standard deviations above the low level baseline, and refer to them as "motion" peaks.

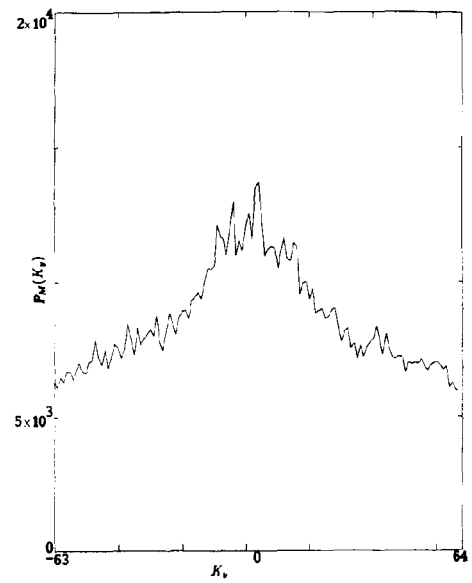

Fig. 2. $P_M(K_y)$, projection of the brain image along K_y.

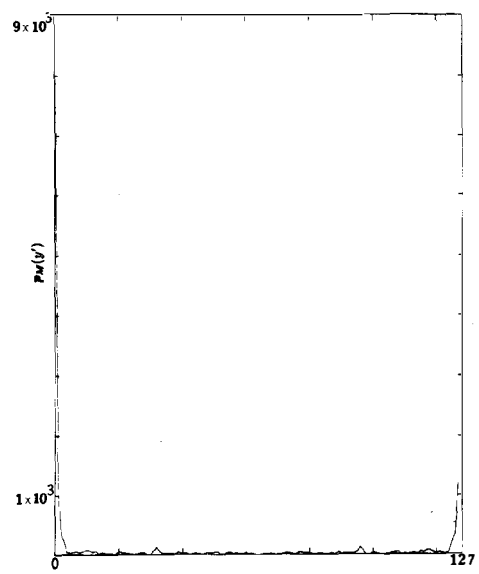

Fig. 3. $p_M(y')$, F^{-1} of brain projection.

3) For the estimation of the motion kernel $G(K_y)$, we follow an approach that retains phase information: We apply a bandreject filter to $p_S(y')$, in order to eliminate "motion" peaks. The bandreject filter (BRF) is unity for

all y' except for a four-point window around each peak. The coefficients of each bandreject window are ($1 \times$ *neighborhood mean / local mean*) for the two center points and ($0.5 \times$ *neighborhood mean / local mean*) for the two others, where by neighborhood mean we mean the magnitude of $p_S(y')$ in the vicinity of the "motion" peak. This bandreject operation produces an estimate of the projection without motion:

$$\tilde{p}_M(y') = \mathrm{BRF}(y')\, p_S(y'). \tag{25}$$

The reason for using the bandreject filter with a four-point window, instead of a simple inverse filter of the form $1/\cos(2\pi f t + \phi)$ is that the single frequency model is very sensitive to errors, and sampling in the frequency domain may result in the effect that some frequencies of the motion may not correspond to the sample frequencies.

4) We obtain an estimate of the projection without motion artifact, $\tilde{P}_M(K_y)$, by taking the Fourier transform of $\tilde{p}_M(y')$.

5) Division of $P_S(K_y)$ with $\tilde{P}_M(K_y)$ yields an estimate, $\hat{G}(K_y)$, for the motion kernel:

$$\frac{P_S(K_y)}{\tilde{P}_M(K_y)} = \hat{G}(K_y) \tag{26}$$

$$\cong \left[1 + \sum_{n=1}^{N} \frac{\Delta m_n}{m_0} \cos(n\omega_y K_y + \phi_n)\right]. \tag{27}$$

Since $P_S(K_y)$ is a motion-degraded projection, it contains all the information about the motion phase. Furthermore, since $\tilde{P}_M(K_y)$ is a "motion-free" projection, the division of $P_S(K_y)$ with $\tilde{P}_M(K_y)$ yields an estimate $\hat{G}(K_y)$ that has the correct motion phase.

6) The motion kernel inverse can then be used to multiply the raw data:

$$\hat{M}(K_x, K_y) = S(K_x, K_y)\, \hat{G}^{-1}(K_y). \tag{28}$$

7) Finally, the restored image $\hat{I}(x, y)$ is simply the inverse transform of the corrected raw data:

$$\hat{I}(x, y) = F^{-1}[\hat{M}(K_x, K_y)]. \tag{29}$$

III. Results

The steps of our algorithm are summarized in Table 1.

The image used for the simulations was a motionless brain image. The raw data were (128×256) and the image was obtained by filling with zeros the top and bottom 64 lines of the raw data and taking the (256×256) inverse Fourier transform. The projection of the raw data along the frequency encoding direction, $P_M(K_y)$, and its inverse Fourier transform are shown in Figs. 2 and 3. We see from Fig. 3 that $p_M(y')$ is highly peaked around the DC and this conforms with our assumption. Note that while taking the 128 point projection, the center 14 columns are zeroed in order to avoid the dominant dc component at the center for scaling purposes. Ghost artifacts were simulated on the image, by multiplying the raw data

TABLE I

1.	Project along $K_x \Rightarrow P_S(K_y)$
2.	$\mathcal{F}^{-1}(P_S(K_y)) \Rightarrow p_S(y')$
3.	Apply bandreject filter to $p_S(y') \Rightarrow \tilde{p}_M(y')$
4.	$\mathcal{F}(\tilde{p}_M(y')) \Rightarrow \tilde{P}_M(K_y)$
5.	Divide $P_S(K_y)$ with $\tilde{P}_M(K_y) \Rightarrow \hat{G}(K_y)$
6.	Multiply $S(K_x, K_y)$ with $\hat{G}^{-1}(K_y) \Rightarrow \hat{S}(K_x, K_y)$
7.	$\mathcal{F}^{-1}(\hat{S}(K_x, K_y)) \Rightarrow \hat{I}(x, y)$

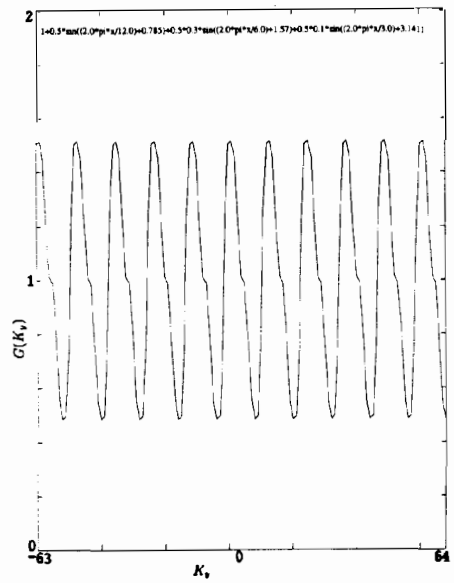

Fig. 4. $G(K_y)$, simulated motion kernel.

along the K_y axis (phase encoding direction) with the function:

$$G(K_y) = 1 + 0.5 \sin\left(\frac{2\pi K_y}{12} + 0.785\right) + 0.15 \sin\left(\frac{2\pi K_y}{6} + 1.57\right) + 0.05 \sin\left(\frac{2\pi K_y}{3} + 3.141\right), \tag{30}$$

which is shown in Fig. 4. Note that this corresponds to truncating (8) after three terms. We detect the motion kernel and correct for the motion artifacts by following the steps described in theory: We project the motion-degraded raw data along the frequency encoding direction and obtain $P_S(K_y)$. By taking the inverse Fourier transform of the projection we obtain $p_S(y')$. $P_S(K_y)$ and $p_S(y')$ are shown in Figs. 5 and 6, respectively. Notice the rather broad peaks around I_1, I_2, and I_3 (the locations of the frequencies of our motion). This is due to the fact

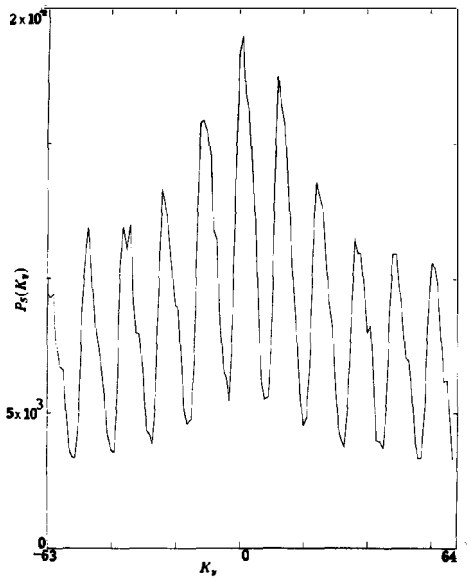

Fig. 5. $P_S(K_y)$, projection of the motion-degraded data along K_y.

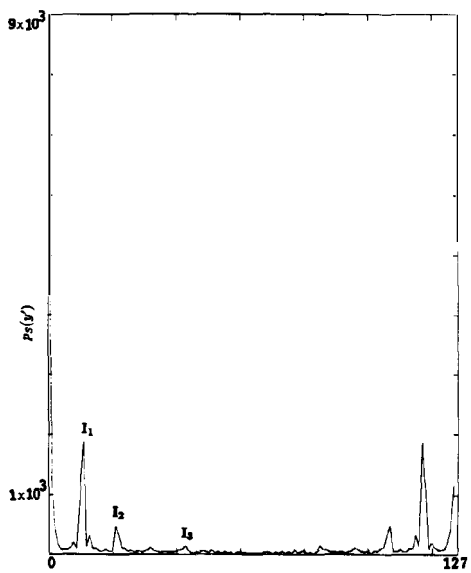

Fig. 6. $p_S(y')$, F^{-1} of $P_S(K_y)$.

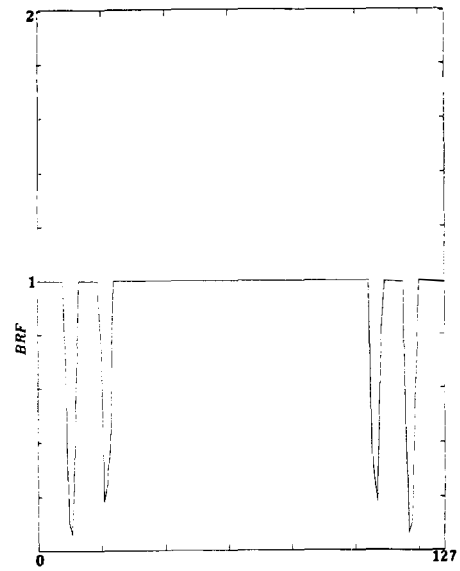

Fig. 7. BRF, bandreject filter.

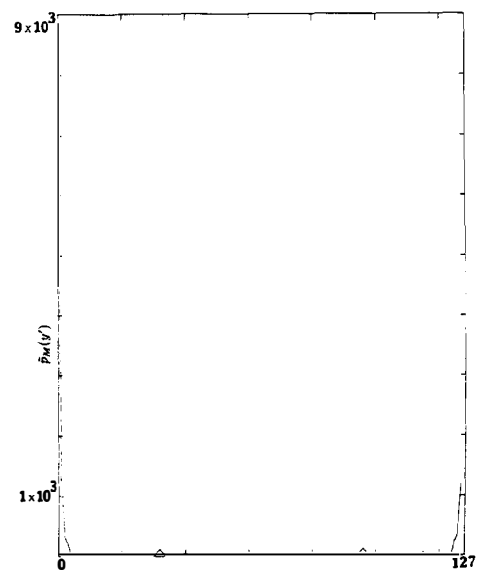

Fig. 8. $\tilde{p}_M(y')$, product of BRF and $p_S(y')$.

that none of the three frequencies of our motion kernel is exactly divisible with 128 (the size of our IFT). Therefore, the energy at f is distributed around the closest integer to $128/f$ where f is a frequency component of the motion kernel.

In order to eliminate the "motion" peaks and obtain $\tilde{p}_M(y')$ we apply a bandreject filter to $p_S(K_y)$ that eliminates I_1 and I_2 because they are two standard deviations above the baseline. I_3 is not being removed because it is not above the two standard deviations limit. The bandreject filter and $\tilde{p}_M(y')$ are shown in Figs. 7 and 8, respectively. The Fourier transform of $\tilde{p}_M(y')$, provides an estimate of the projection without motion artifact, $\tilde{P}_M(K_y)$, which is shown in Fig. 9. The estimate for the motion kernel, $G(K_y)$, is obtained by division of $P_S(y')$ with $\tilde{P}_M(K_y)$, and is shown in Fig. 10. The small deviation from 1 of the ratio $G(K_y)/\hat{G}(K_y)$ (Fig. 11), shows that the motion kernel was estimated with reasonable accuracy.

Finally, as shown in steps (6) and (7) of Table 1, we multiply the raw data with the inverse of the motion kernel estimate and the restored image is just the inverse Fourier transform of the corrected raw data. In Fig. 12 we show the projection of the corrected raw data, which as

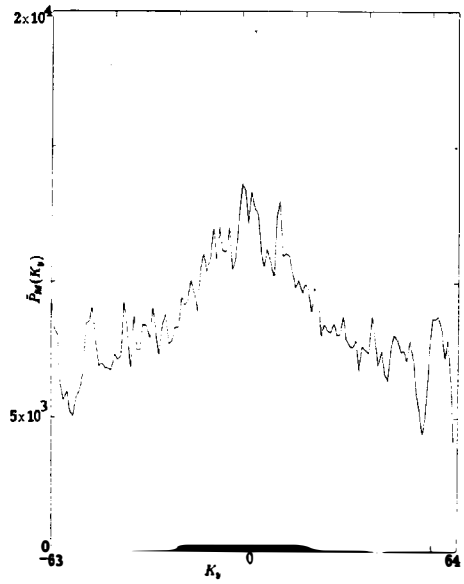

Fig. 9. $\tilde{P}_M(K_y)$, "filtered" projection.

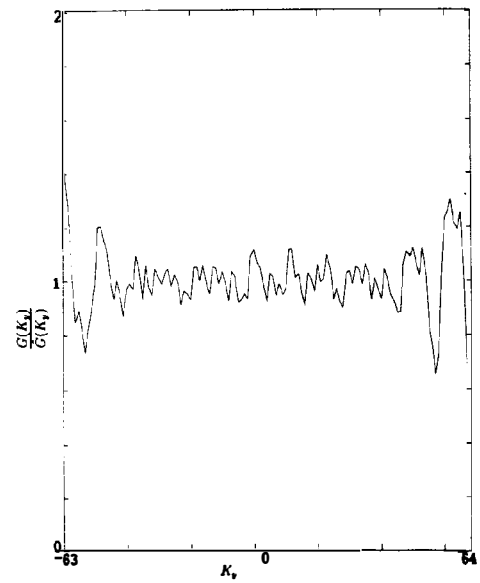

Fig. 11. Deviation from 1 of the ratio $G(K_y)/\hat{G}(K_y)$.

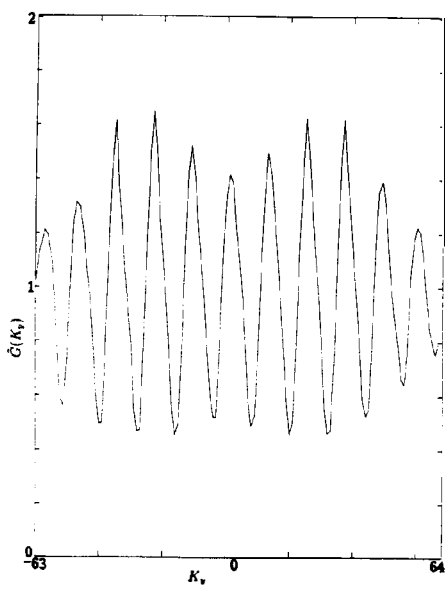

Fig. 10. $\hat{G}(K_y)$, estimated motion kernel.

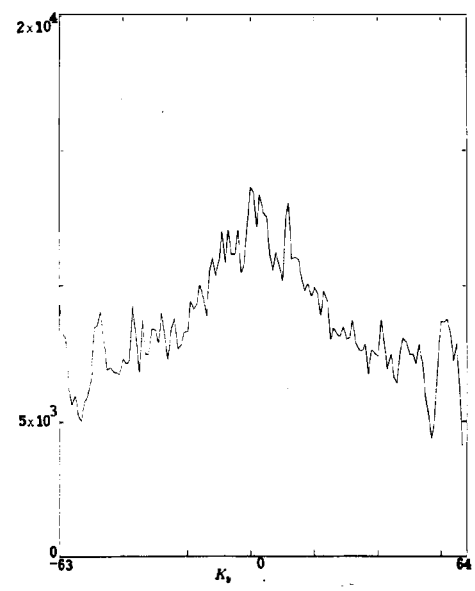

Fig. 12. Projection along K_y of the restored image $\hat{I}(x, y)$.

expected is the same as $\tilde{P}_M(K_y)$. In Figs. (13), (14), and (15) we show, respectively, the original, motion-degraded, and corrected brain images. In Figs. (16), (17), and (18) we show the above images in the same order but at higher contrast.

IV. Discussion

A simple model for periodic motion of a single slice along the slice selection axis shows that the "ghost" images result from amplitude modulation of the raw data. This modulation can be detected by inspection of the one-dimensional transform of the magnitude of the complex data. This is somewhat analogous to the well known cepstral analysis [8], where a *log* operation would be applied to the magnitude projection. In our case, that *log* operation is not necessary and does not add to the detectability.

It is also interesting to note that if we were to take the transform of the projection of the power spectrum (magnitude square as opposed to the magnitude), then by the projection slice theorem this would be equivalent to examining the intensity autocorrelation of the image along

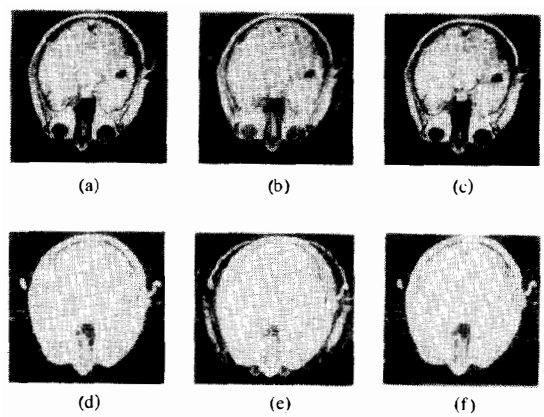

Fig. 13. a) Brain image, normal contrast. b) Motion-degraded image, normal contrast c) Restored image $\hat{f}(x, y)$, normal contrast. d) Brain image, high contrast. e) Motion-degraded image, high contrast. f) Restored image $\hat{f}(x, y)$, high contrast.

the y axis. Again, this is not done since the information we seek is explicitly on the magnitude spectrum and its related functions. The procedure outlined has worked well when the artifact is imposed on otherwise motion-free clinical scans. A number of issues remain to be explored before the technique can be exploited clinically, however. Some concerns are: a) periodic versus nonperiodic motion in patients, b) shift-invariant versus shift-varying motion, c) minimum detectability of $\Delta m_n / m_0$ in design of bandreject filter, d) finite slice-thickness, and contamination of the signal from structures in adjacent slices.

Also, the lack of analogous compensation for the more difficult cases of x and y motion may limit the applicability of this algorithm, since compound motions are likely in practice. Research continues on these and related issues. The z motion correction algorithm is a preliminary step in a large and serious problem in MRI, and the initial results are encouraging.

References

[1] M. L. Wood and R. M. Henkelman, "MR image artifacts from periodic motion," *Med. Phys.*, vol. 12, pp. 143–151, Apr. 1985.

[2] D. R. Bailes, D. J. Gilderdale, G. M. Bydder, A. G. Collins and D. N. Firmin, "Respiratory ordered phase encoding: A method for reducing respiratory motion artefacts in MR imaging," *J. Comp. Assist. Tomography*, vol. 9, no. 4, pp. 835–838, Jul./Aug. 1985.

[3] P. M. Pattany, *et al.*, "Motion artifact suppression technique for MR imaging," *J. Comp. Assist. Tomography*, vol. 11, no. 3, pp. 369–377, May/Jun. 1987.

[4] M. L. Wood, V. M. Runge, and R. M. Henkelman, "Overcoming motion in abdominal MR imaging," *AJR*, vol. 150, pp. 513–522, Mar. 1988.

[5] R. L. Ehman and J. P. Felmlee, "Adaptive technique for high-definition MR imaging of moving structures," *Radiology*, vol. 173, no. 1, pp. 255–263, Oct. 1989.

[6] S. W. Young, *Magnetic Resonance Imaging*. New York: Raven Press, 1988.

[7] S. J. Riederer, "Recent advances in magnetic resonance imaging," *Proc. IEEE*, vol. 76, no. 9, pp. 1095–1105, Sept. 1988.

[8] A. V. Oppenheim and R. Schafer, *Discrete Time Signal Processing*. Englewood Cliffs, NJ: Prentice Hall, 1989, Ch. 11.